Vehicle-induced aerodynamic loads on highway sound barriers part 2: numerical and theoretical investigation

Dalei Wang, Benjin Wang and Airong Chen [*]

Department of Bridge Engineering, Tongji University, Shanghai, 200092, China

Abstract. The vehicle-induced aerodynamic loads bring vibrations to some of the highway sound barriers, for they are designed in consideration of natural wind loads only. As references to the previous field experiment, the vehicle-induced aerodynamic loads is investigated by numerical and theoretical methodologies. The numerical results are compared to the experimental one and proved to be available. By analyzing the flow field achieved in the numerical simulation, the potential flow is proved to be the main source of both head and wake impact, so the theoretical model is also validated. The results from the two methodologies show that the shorter vehicle length would produce larger negative pressure peak as the head impact and wake impact overlapping with each other, and together with the fast speed, it would lead to a wake without vortex shedding, which makes the potential hypothesis more accurate. It also proves the expectation in vehicle-induced aerodynamic loads on Highway Sound Barriers Part1: Field Experiment, that max/min pressure is proportional to the square of vehicle speed and inverse square of separation distance.

Keywords: vehicle-induced aerodynamic loads; highway sound barriers; numerical simulation; theoretical model; potential theory

1. Introduction

In vehicle-induced aerodynamic loads on Highway Sound Barriers Part1: Field Experiment (abbreviated as P1 in the following), the effect of vehicle-induced aerodynamic loads was illustrated based on the experimental results. However, the experiment only provided the phenomenon and was not sufficient to give the prediction without explanation of the mechanism. It is necessary to explore other methodologies to predict the effect and to reveal the mechanism.

Firstly, the numerical simulation was adopted. Though limited researches were achieved in this problem before, some methodologies in similar fields (Waymel *et al*. 2006, Corin *et al*. 2008, Hemida and Baker 2010) were found helpful in developing the numerical simulation here. Another way to solve the problem was the theoretical analysis. Sanz-Andrés *et al*. (2002, 2003, 2004) proposed the solution to the vehicle-induced aerodynamic loads on signs and pedestrians based on potential theory. Then Barrero-Gil and Sanz-Andrés (2009) take the flexibility of panel into account and perceived that the aeroelastic effect cannot be neglected for it produces secondary

---

∗Corresponding author, Professor, E-mail: a.chen@tongji.edu.cn

load cycles. Inspired by the previous studies, a theoretical model of vehicle-induced aerodynamic loads on sound barriers was established based on the potential theory.

Works reported here is focused on the numerical and theoretical way to study the vehicle-induced aerodynamic loads on highway sound barriers. By these two methodologies, the time-history of vehicle-induced aerodynamic loads on highway sound barriers and the flow field are reproduced under the same conditions in P1. Then the variables are discussed based on the theoretical model and the flow field achieved by numerical way.

2. Numerical simulation

The numerical simulation was based on fluid analysis software FLUENT, and all computational domains were established referring to the field experimental cases.

2.1 Basic governing equations

The mathematical model of the flow field must obey the governing equations based on the mass conservation law, momentum conservation law and energy conservation law, shown as follows by Eqs. (1)- (3)

Continuity equation:
$$\frac{\partial \rho}{\partial t} + \mathrm{div}(\rho U) = 0 \tag{1}$$

Navier-Stokes equation:
$$\frac{\partial u}{\partial t} + \mathrm{div}(uU) = \mathrm{div}(\upsilon \mathbf{grad}u) - \frac{1}{\rho}\frac{\partial p}{\partial x} + S_u$$
$$\frac{\partial v}{\partial t} + \mathrm{div}(vU) = \mathrm{div}(\upsilon \mathbf{grad}v) - \frac{1}{\rho}\frac{\partial p}{\partial y} + S_v \tag{2}$$
$$\frac{\partial w}{\partial t} + \mathrm{div}(wU) = \mathrm{div}(\upsilon \mathbf{grad}w) - \frac{1}{\rho}\frac{\partial p}{\partial z} + S_w$$

Energy equation:
$$\frac{\partial(\rho T)}{\partial t} + \mathrm{div}(\rho UT) = \mathrm{div}(\frac{k}{c_p}\mathbf{grad}T) + S_T \tag{3}$$

Since most of the flow fields in engineering are turbulent, the nonlinear Navier-Stokes equation is difficult to solve directly. The complicated turbulent flow needs very small scale grids, so that the computational conditions become too high to approach. Therefore, a turbulence model is necessary to simplify the solution.

2.2 Turbulence model

Based on the conception that the average variations of the flow field rather than the transient ones are important in engineering, a practical Reynolds Average Method (also called RANS) is put forward. The averaging introduces more variables and needs supplementary equations. The standard $k - \varepsilon$ model and its derivative models (RNG $k - \varepsilon$ & realizable $k - \varepsilon$) add two

equations about kinetic energy of turbulence (k) and turbulent dissipation rate (ε) to help solving the variables. A test was taken to find out the applicability of RNG $k-\varepsilon$ model and realizable $k-\varepsilon$ model in this problem by using them to calculate pressures on measuring point $10^{\#}$ as defined in P1 at an ultimate state. The test case assumed a Kinglong Coach passed by the sound barrier at the speed of 120 km/h with the minimum distance of 0.75 m. The comparison of the results shows in Fig. 1, which indicates that the two turbulence models won't make great difference (3% in maximum), and the realizable $k-\varepsilon$ model is the final choice in this paper.
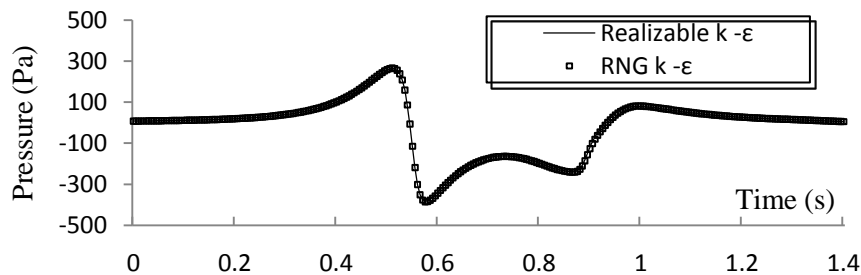

Fig. 1 Comparison of results from realizable $k-\varepsilon$ model and RNG $k-\varepsilon$ model
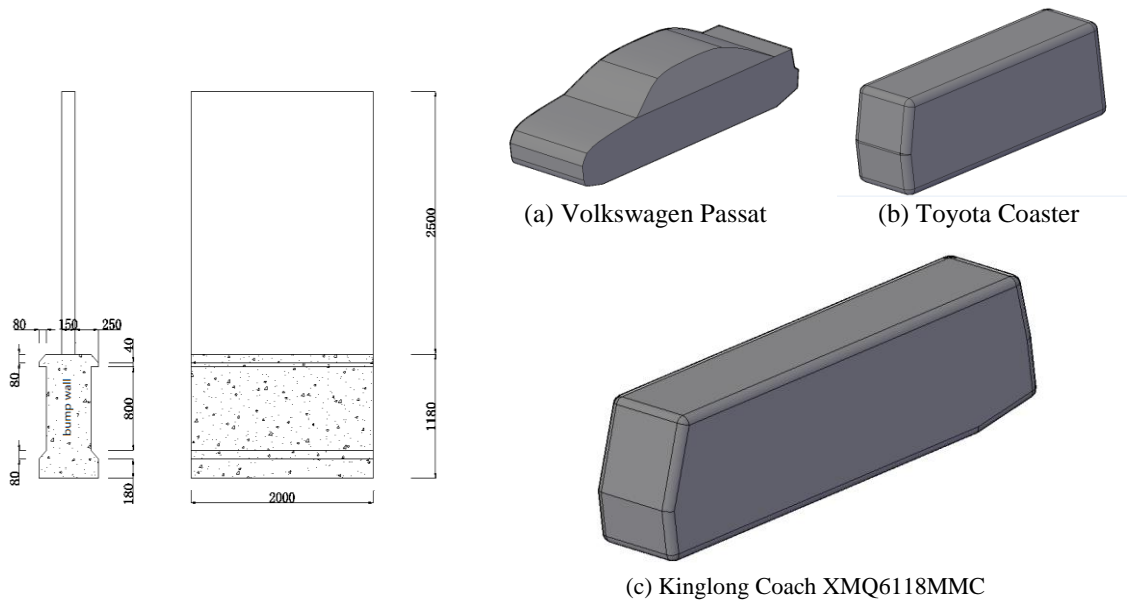

(a) Volkswagen Passat

(b) Toyota Coaster

(c) Kinglong Coach XMQ6118MMC

Fig. 2 A 2 m long section of sound barriers in computational domain

Fig. 3 Geometric model of typical vehicles

2.3 Geometric model

The three-dimensional geometric models of flow fields were established in AutoCAD. To reach

a general conclusion for all kinds of sound barriers, the barrier bodies were created in a shape of flat board instead of the experimental one. The columns were ignored, while the shape of the concrete bump wall was taken into account. The sound barriers and bump walls were built in full-length in the computational domain. A 2 m long section of sound barrier is taken for instance in Fig. 2.

Fig. 3 gives out the vehicles' three-dimensional geometric models. In order to balance the computational accuracy and efficiency, the build was mainly focused on the vehicular profile, such as the chamfering on the edges, bevel of fore window, whereas the tires, rearview mirror, wipers, door handles and some other details were ignored. Removing the tires seemed to be a noticeable change of vehicle shape, but the effect caused by tires was negligible in calculating the pressure on sound barriers, since the tires were much lower than the sound barriers.

2.4 Computational domain mesh and boundary conditions

The computational domain should be sufficient to make vehicle-surrounding flow field fully developed before it reaches the focus section. Considering the computational conditions we have, an 80 m×40 m×15 m computational domain was determined. To simulate the motion of vehicles, the dynamic layering model was used locally, which was specified to an 80 m×4 m×5 m region. The dynamic layering model would move the grids by splitting or merging the grids next to the boundary, on condition that the grid heights are greater or less than a user-defined value. The velocity of grids movement was controlled by UDF (User Defined Function) in FLUENT.

The mesh was done by pre-processing software ICEM-CFD. Benefited by the simplified geometric model, the whole computational domain was meshed to hexahedral grids with high quality and efficiency. The dynamic mesh region and the static mesh region could be meshed separately, and the boundary condition of interface in FLUENT was applied to the two regions, by which data could exchange between regions with non-conformal mesh.

A 2m long section of sound barrier in the middle of the computational domain was chosen to be the focus section, on which the pressure was monitored. Around the focus section, the grids were dense, while the regions far from it were meshed in a relative coarse way. As a result, the minimum volume of the grids was $1.39×10^{-5} \text{m}^3$, while the maximum one was $1.02×10^{-1} \text{m}^3$. The overall number of grids was about 5 million, involving 1.4~1.7 million (due to the different vehicle types) in the dynamic region.

Table 1 Summary of boundary conditions

	Boundary condition
Right side	Velocity inlet
Left side	Pressure outlet
Vehicle, sound barrier, ground	Wall
Front/back side, top side	Symmetry
Boundary of dynamic mesh region	Interface

Table 1 shows all the boundary conditions in the computational domain. The setups of velocity inlet and pressure outlet were for the pressure balance of the entire computational domain to avoid

calculating divergence. As the vehicle-induced aerodynamic loads rather than the natural one is the focus issue in this paper, the velocity was only set to 1×10^{-2}m/s, while turbulent kinetic energy and turbulent dissipation rate were set to 1×10^{-4}m^2/s^2 and to 1×10^{-4}m^2/s^3, respectively.
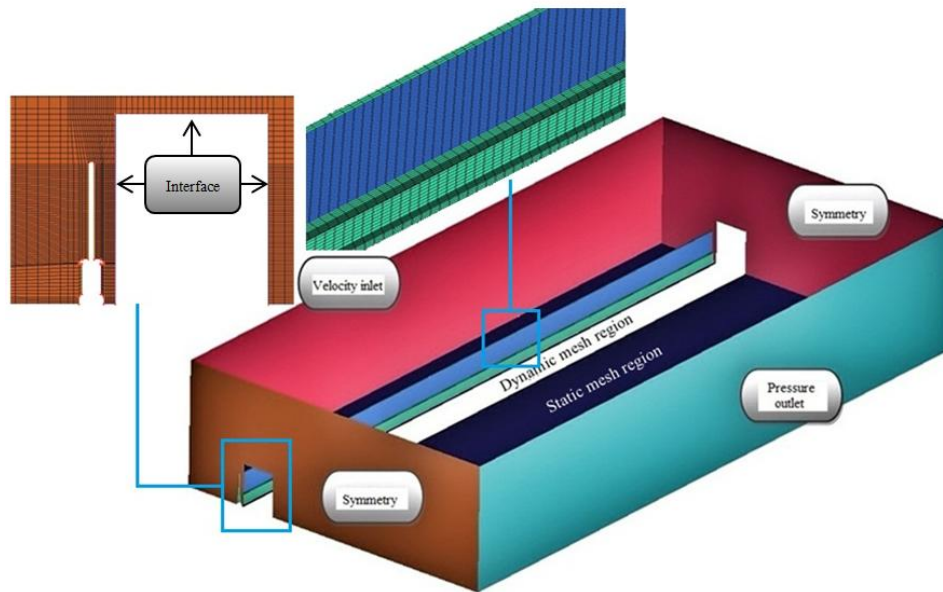

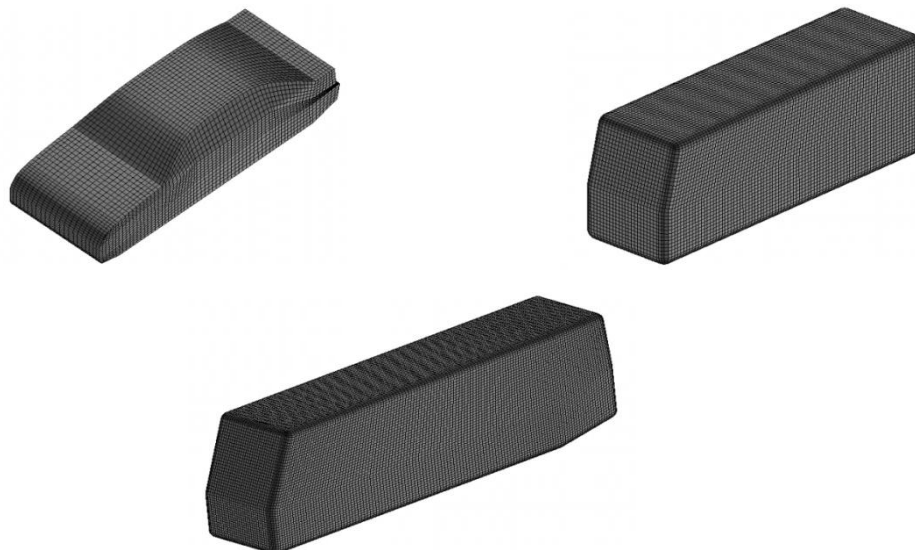Fig. 4 Mesh around sound barriers and boundary conditions

Fig. 5 Mesh around vehicles

2.5 Solution method and time step

The pressure-based solver with SIMPLE (Semi-implicit method for pressure-linked equations) algorithm was used, and the discretization for the convective terms and diffusive terms were the first order upwind scheme and central differencing scheme, respectively. It is believed that the second order upwind scheme could make a better approach and thus is commonly used in CFD projects. But due to a test case (under the same conditions to the one in Chapter 3.4), the two schemes got very similar results except a little difference in the second negative peak, as shown in Fig. 6. Therefore, the first order upwind scheme was adopted in this paper because of its higher calculation efficiency.
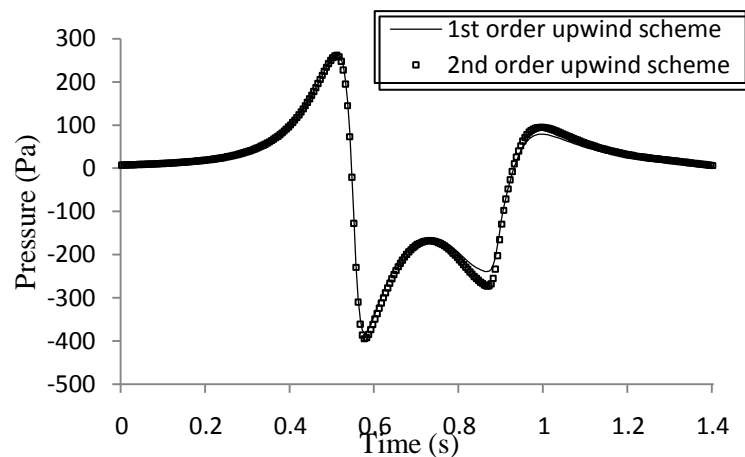

Fig. 6 Comparison of results from the first/second order upwind scheme

Table 2 Summary of numerical simulation schemes and parameters

Discretization of governing equations	Finite volume method
Size of computational domain	80 m×40 m×1 5m
Types of grids	Hexahedral
Total number of grids	About 5 millions
Dynamic mesh method	Dynamic layering model
Turbulence model	Realizable $k-\varepsilon$
Discretization of convection term	First order upwind scheme
Discretization of diffusion term	First order central difference scheme
Algorithm	SIMPLE
Time step length	0.005s

Due to the dynamic layering model that is used in dynamic mesh region, the vehicle speed and grids' height on the grid generating/removing surface should be taken into account in determining the length of time steps, which is ruled by the following formula

$$\Delta t \times v \le \frac{\Delta l}{2} \tag{4}$$

where Δt is the length of time steps, v is the vehicle speed, Δl is the critical value for splitting or merging grids. As the grid heights on the boundary were about 0.1m, Δl is set to be 0.1, thus Δt is set to be 0.005s to meet Eq. (4).

Table 2 gives out the main schemes and parameters in numerical simulation.

3. Theoretical model

The theoretical model was established on assumptions similar to the ones proposed by Sanz-Andrés *et al*. (2002, 2003, 2004). It can be solved by theory of potential flows but with inaccurate results since the vehicles' body shapes can't be described theoretically, therefore a calibration is needed. Then the theoretical model consequently lead to an equation which provides a very simple but effective way to calculate the vehicle-induced aerodynamic loads on highway sound barriers.

3.1 Hypothesis

(1) The flow generated by the vehicle motion is a potential flow, both in the field influenced by the vehicle head and wake. Here the wake part should not be neglected for the wake impact plays an important role in vehicle-induced aerodynamic loads. Even though it is not showing purely potential features, the potential hypothesis is able to develop a practical way to achieve the accurate result.

(2) The potential flow generated by the vehicle is represented as the combination of a point source and a point sink. The former one locates on the vehicle head, with intensity Q_1, which is determined by the vehicle speed and cross-sectional area. The latter one is at the end of the vehicle, with intensity Q_2, which is dependent on Q_1.

(3) The sound barrier is considered as a plate with very large area but little thickness, and the vibration of it could be ignored, which makes a boundary condition of wall in the model.

(4) The pressure field is determined by using the non-steady potential flow Bernoulli Equation.

3.2 Modeling

Take the origin in the coordinate system as the focus point, the model is described in Fig. 7. The vehicle is represented as a box in dash line, moving towards the negative direction of x-axis in a speed of v.

As the experimental results concluded that the vehicle-induced aerodynamic loads consists of head impact and wake impact, the flow generated by the vehicle could be represented as that produced by a moving point source, followed by a moving point sink. The point source intensity Q_1 is determined by the vehicle speed and cross-sectional area, while the point sink intensity Q_2 is dependent on Q_1.

The original longitudinal position of the point source is b, while the horizontal source-barrier separation distance is d, the vertical source-barrier separation distance is h. Therefore, after a period time of t, the coordinate of the point source would be *(-b+vt, d, h)*, while the one of point

sink would be *(-b-l+vt, d, h)*. Now that the sound barrier is considered a boundary condition of wall, the image source/sink should be positioned symmetrical to the xz-plane, and the coordinate of the image source/sink would be *(-b+vt, d, h)* and *(-b-l+vt, -d, h)*.
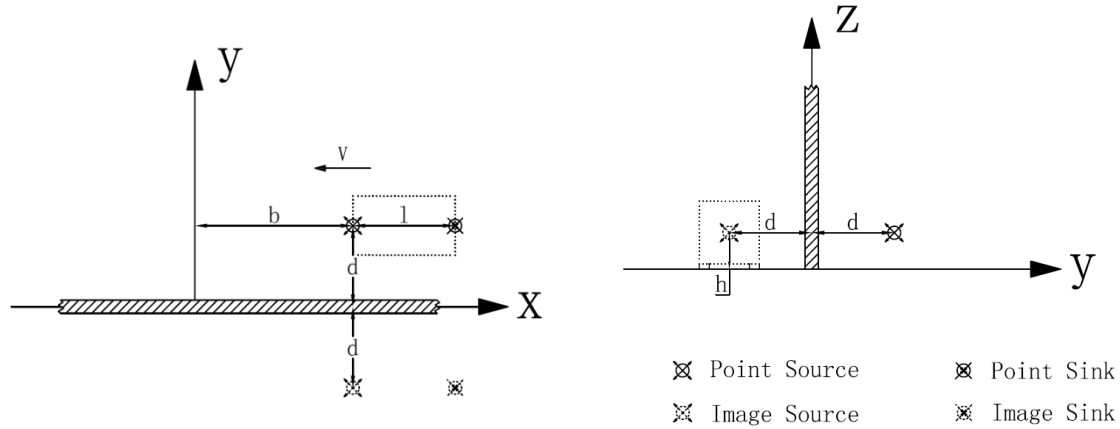

Fig. 7 Schematic layout of the model

Following the theory of potential flow, the potential functions in the flow field are as showing below, in which φ_1, φ_1' are for the point source and its image, φ_2, φ_2' are for the point sink and its image.

$$\begin{cases} \varphi_1(x,y,z,t) = \dfrac{Q_1}{4\pi} \cdot \left[\dfrac{1}{\sqrt{(x-b+vt)^2+(y-d)^2+(z-h)^2}}\right] \\[4mm] \varphi_1'(x,y,z,t) = \dfrac{Q_1}{4\pi} \cdot \left[\dfrac{1}{\sqrt{(x-b+vt)^2+(y+d)^2+(z-h)^2}}\right] \\[4mm] \varphi_2(x,y,z,t) = \dfrac{Q_2}{4\pi} \cdot \left[\dfrac{1}{\sqrt{(x-b-l+vt)^2+(y-d)^2+(z-h)^2}}\right] \\[4mm] \varphi_2'(x,y,z,t) = \dfrac{Q_2}{4\pi} \cdot \left[\dfrac{1}{\sqrt{(x-b-l+vt)^2+(y+d)^2+(z-h)^2}}\right] \end{cases} \tag{5}$$

where $Q_1 = c_1 vA$, v is the vehicle speed, A is the cross-sectional area, $Q_2 = c_2 Q_1$, $c_2 < 0$.

The potential function of the upper half flow field would be the superposition of φ_1, φ_1', φ_2, φ_2'.

$$\varphi(x,y,z,t) = \varphi_1 + \varphi_1' + \varphi_2 + \varphi_2' \tag{6}$$

At the focus point *(0, 0⁺, 0)*

$$\begin{cases} u = \dfrac{\partial \varphi}{\partial x}\Big|_{(0,0^+,0)} = \dfrac{Q_1}{4\pi}\left\{\dfrac{2(b-vt)}{\left[(-b+vt)^2+d^2+z_0^2\right]^{3/2}} + c_2 \cdot \dfrac{2(b+l-vt)}{\left[(-b-l+vt)^2+d^2+z_0^2\right]^{3/2}}\right\} \\[3mm] v = \dfrac{\partial \varphi}{\partial y}\Big|_{(0,0^+,0)} = 0 \\[3mm] w = \dfrac{\partial \varphi}{\partial z}\Big|_{(0,0^+,0)} = \dfrac{Q_1}{4\pi}\left\{\dfrac{2z_0}{\left[(-b+vt)^2+d^2+z_0^2\right]^{3/2}} + c_2 \cdot \dfrac{2z_0}{\left[(-b-l+vt)^2+d^2+z_0^2\right]^{3/2}}\right\} \\[3mm] \dfrac{\partial \varphi}{\partial t}\Big|_{(0,0^+,0)} = \dfrac{Q_1}{4\pi}\left\{\dfrac{2v(-b+vt)}{\left[(-b+vt)^2+d^2+z_0^2\right]^{3/2}} + c_2 \cdot \dfrac{2v(-b-l+vt)}{\left[(-b-l+vt)^2+d^2+z_0^2\right]^{3/2}}\right\} \end{cases} \tag{7}$$

where *u, v, w* are the velocity component in x, y, z axis, respectively.

As for the point *(0, 0⁻, 0)*, all the velocity components would be zero, since the potential function in the lower half flow field is the constant of zero.

The non-steady potential flow Bernoulli Equation is

$$P + \frac{1}{2}\rho V^2 + \rho\frac{\partial \varphi}{\partial t} = C \tag{8}$$

where *P* is the pressure, $V = \sqrt{u^2 + v^2 + w^2}$, ρ is the density of air, *C* is a constant.

By introducing Eq. (7) to Eq. (8), the pressure difference between the point *(0, 0⁺, 0)* and *(0, 0⁻, 0)* is given in

$$\Delta P = -\frac{1}{2}\rho V^2 - \rho\frac{\partial \varphi}{\partial t} \tag{9}$$

Table 3 Calibration coefficients of typical vehicles

Vehicle type	c_1	c_2	c_3
KC	1.8	-0.5	1
TC	1.8	-0.5	1.15
VP	1.7	-0.7	0.9

3.3 Model calibration

Since the vehicle is simplified to point source & sink, the vehicle shape is not taken into consideration. Therefore, the intensity of the point source/sink should be modified, with the coefficient c_1, c_2, which are only influenced by the vehicle shape, and the values can be achieved by the numerical results, as shown in Table 3.

Besides, the interval between the head impact and wake impact is not precisely the vehicle length (see P1), so it might lead to some errors in predicting the pressures, especially for the VP

cases. By calculating R_t as P1 defined and the flow field showing in Fig. 11, a coefficient c_3 is introduced to calibrate the distance between point source and point sink, i.e., $l = c_3 \cdot L_0$, where L_0 is the vehicle length.

4. Results and discussion

4.1 Time-history of pressures

In P1, the conditions in field experimental cases and the results were already given. By choosing typical values of variables in field experiment, a total of eight cases (KC-2, 4, 5, & TC-1, 4, 7, & VP-1, 4) were taken into selective analysis, which would investigate these cases in numerical and theoretical ways.
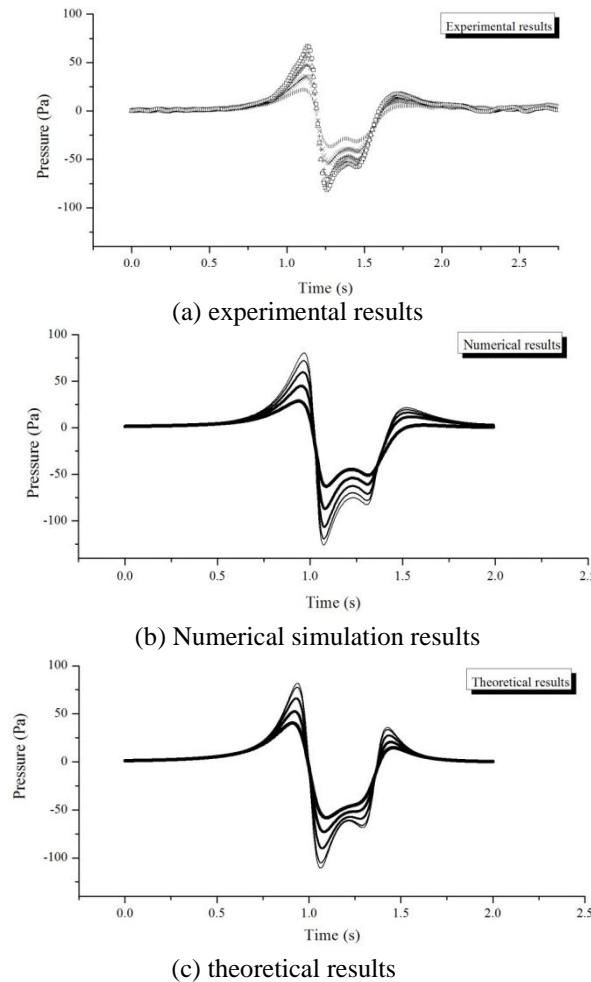

(a) experimental results

(b) Numerical simulation results

(c) theoretical results

Fig. 8 Comparison of experimental, numerical and theoretical results on measuring point $6^{\#} \sim 10^{\#}$ of case TC-1

Take case TC-1 for instance, Fig. 8 shows the numerical and theoretical results on different locations in comparison of the experimental ones. The theoretical results are not so precise on higher measuring points (see the bolder lines in Fig. 8), which is attributed to the wall boundary in theoretical model for separating the two sides of sound barrier completely. Nevertheless, the time-history trend is almost consistent, which means the time-history curves on one point will be enough to illustrate the whole process. Pressures on measuring point $10^{\#}$ collected by three methodologies will be shown and discussed in the following.

Because of the similarities of the pressure time-history curves in KC & TC cases, results of KC & TC cases are put together in Fig. 9. Noticing that the time spans in the three methodologies are different, the origin of time is chosen to be the one in numerical simulation. Thus negative time may appear in some curves, and the same to the following figures.

(a) KC-2
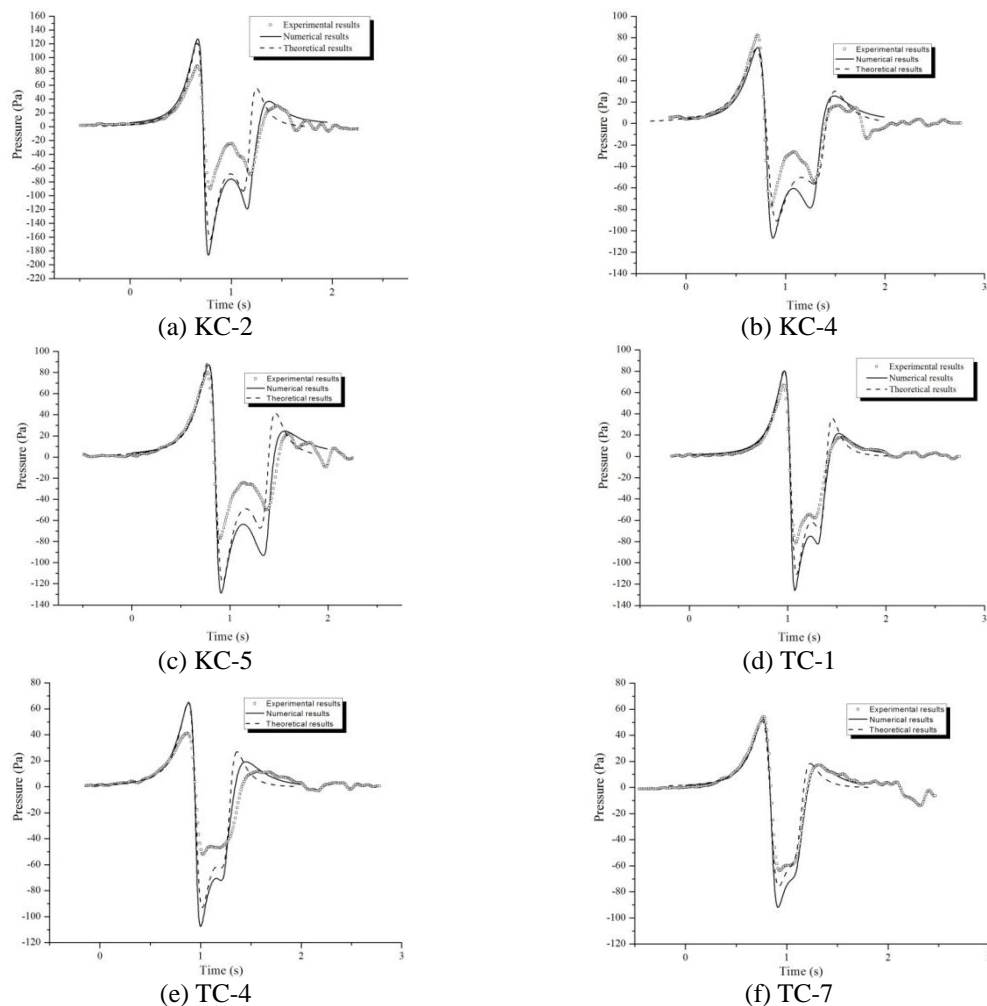
(b) KC-4

(c) KC-5

(d) TC-1

(e) TC-4

(f) TC-7

Fig. 9 Comparison of experimental, numerical and theoretical results of KC & TC cases

The numerical results appear to be beyond the experimental ones, especially in the negative peak. The main reason could be the personal error in driving vehicles. It is hard for the drivers to keep the distance close enough to meet the plan exactly due to the concern of risks, so the bigger distances make the lower pressures in the experiment. Therefore, the numerical results show stronger regularities in all cases, which is the reason why the calibration of theoretical model is based on it.

The theoretical results are in great agreement with the numerical one in head impact part, but with slight differences in the wake impact part. It is consistent to previous studies, showing that wake impact is influenced by the vortex shedding and reattachment rather than an effect caused by pure potential flow. However, the potential hypothesis is still helpful for the simple form of solution with acceptable error, even in the part of wake impact.

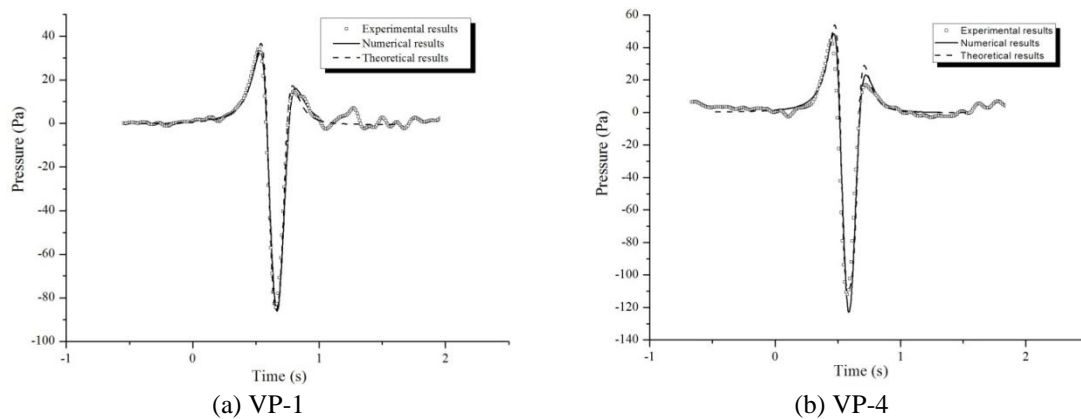(a) VP-1   (b) VP-4

Fig. 10 Comparison of experimental, numerical and theoretical results of VP cases

Due to the streamlined vehicle shape of VP, the results are obviously different from other vehicles. Apparently seen in Fig. 10, the pressure time-history curves of VP cases significantly vary from other cases with only one negative peak with a much greater value compared to the positive one, which can be attributed to the head impact and wake impact overlapped each other.

The numerical results of VP cases show great agreement with experimental ones. By the benefits from Volkswagen Passat's low position of cab and small width of vehicle body, the distances are more controllable than other vehicles. Therefore the personal error in the experiment decreased, so as to meet the situations in numerical simulation more perfectly.

The theoretical model explains how the extremely large negative peak is produced, and its results of VP cases are accurate comparing to the experimental and numerical results, showing that it is a practical and effective way in solving this problem.

4.2 Flow field analysis

The methodologies of numerical and theoretical would gain not only the time-history of pressure, but also the solution of the whole flow field. The streamline pattern in numerical simulation is shown in Fig. 11. It is observed that the flow field is similar to potential one, as the

streamlines converge near the vehicle head and end, just the same to the effect of the point source and point sink.

The vortex shedding can be certainly observed in the wake of KC and TC, but not in that of VP, at least in a range of two times of vehicle length. It can be mainly attribute to the streamlined shape and fast speed in VP cases, which, to a certain level, is identical to the hypothesis that "the pass is so quick that there is not time enough for a wake to be developed on the flow behind the barrier", proposed by Sanz-Andrés *et al*. (2004). Besides, the flow obviously separates on the top of the sound barrier in Fig. 11, which proves that the different boundary condition caused the numerical results differs from the theoretical ones on higher measuring points, as mentioned before.
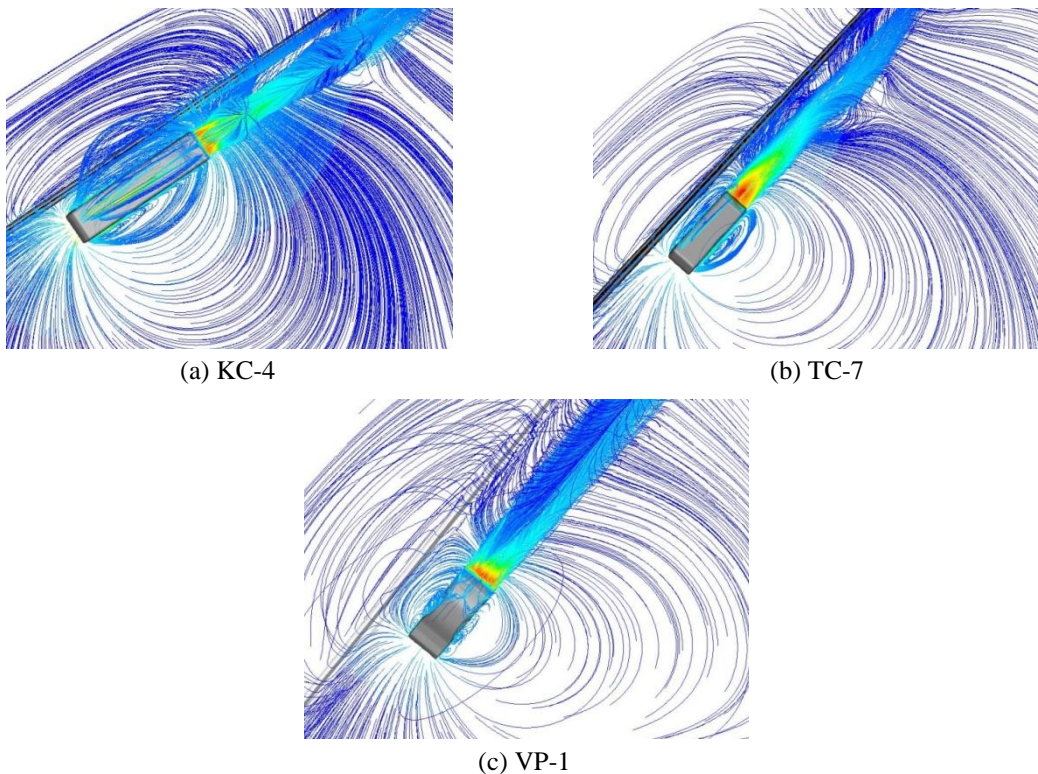

(a) KC-4　　　　　　　　　　　　　　　　　(b) TC-7

(c) VP-1

Fig. 11 Typical streamlines around vehicles and sound barriers

4.3 Discussion on variables

By carrying out the discussions above, the theoretical results are considered practical and effective in predicting the time-history of pressures, at least in the positive and negative peak. Therefore the theoretical model is able to reveal the effect of variables such as vehicle type and vehicle speed.

The vehicle type consists of the shape, length and cross-sectional area. The former two are

included in the calibration coefficients, c_1, c_2, c_3, while the last one is included in the source/sink intensity. As Table 3 presents, c_1 & c_2 for streamlined vehicles would certainly be smaller, because of the weaker head impact and stronger wake impact. However, the coefficient c_3 is difficult to determine, for the streamline converge to an area rather than a point as Fig. 11 represents, therefore the value of c_3 is experiential ones here.

As for the vehicle speed and vehicle-barrier separation distance, the Eq. (9) already describes their relation to the pressure. The max/min pressure changes with vehicle speed and separation distance (from the point source to the barrier), as shown in Figs. 12 and 13 respectivley. The separation distance is only concentrated on the horizontal one for the source is set at the same height as the focus point, so that the vertical separation distance is zero, i.e., h = 0 m. Since the results are based on the potential theory, it is not surprise that the max/min pressure is proportional to the square of vehicle speed and inverse square of separation distance.
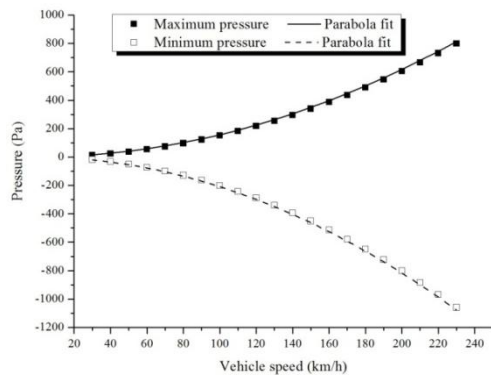

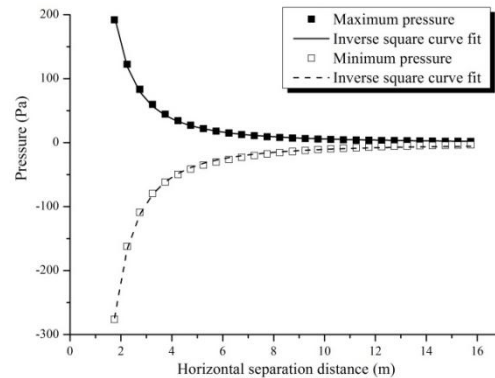Fig. 12 Variation of max/min pressure with vehicle speed (KC type, d=1.745 m)

Fig. 13 Variation of max/min pressure with horizontal separation distance (KC type, V=90 km/h, h=0 m)

5. Conclusions

The numerical approach using FLUENT and the theoretical one based on potential theory are developed to study the vehicle-induced aerodynamic loads on highway sound barriers. Since the numerical and theoretical results are both in good agreement to the experimental ones, it is possible to predict the effect of vehicle-induced aerodynamic loads on sound barriers, and to investigate the mechanism of it.

The effects of head impact and the wake impact defined in P1 can be identically generated by a point source together with a point sink in theoretical model. By analyzing the flow field achieved in the numerical simulation, the potential flow is proved to be the main source of both head and wake impact. Therefore the theoretical model is effective and practical, with acceptable errors. However, the model requires calibration that is related to the vehicle shape, so the coefficients provided here is only available for the three vehicle types. Further study is still needed.

Through the analysis of flow field and the discussion on variables, the following can be concluded: (1) the shorter vehicle length would produce large negative pressure peak as the head

impact and wake impact overlapping with each other; (2) the fast speed and short vehicle length would lead to a wake without vortex shedding, which means more potential feature in that case; (3) the max/min pressure is proportional to the square of vehicle speed and inverse square of separation distance.

Acknowledgements

References

Baker, C. J. (2001), "Flow and dispersion in ground vehicle wakes", *J. Fluid. Struct.*, **15**(7), 1031-1060.

Baker, C. (2010), "The flow around high speed trains", *J. Wind Eng. Ind. Aerod.*, **98**(6-7), 277-298.

Barrero-Gil, A. and Sanz-Andrés, A. (2009), "Aeroelastic effects in a traffic sign panel induced by a passing vehicle", *J. Wind Eng. Ind. Aerod.*, **97**(5-6), 298-303.

Cali, P.M. and Covert, E.E. (2000), "Experimental measurements of the loads induced on an overhead highway sign structure by vehicle-induced gusts", *J. Wind Eng. Ind. Aerod.*, **84**(1), 87-100.

Corin, R.J., He, L. and Dominy, R.G. (2008), "A CFD investigation into the transient aerodynamic forces on overtaking road vehicle models", *J. Wind Eng. Ind. Aerod.*, **96**(8-9), 1390-1411.

Fujii, K. and Ogawa, T. (1995), "Aerodynamics of high speed trains passing by each other", *Comput. Fluids*, **24**(8), 897-908.

Gerhardt, H.J. and Krüger, O. (1998), "Wind and train driven air movements in train stations", *J. Wind Eng. Ind. Aerod.*, **74-76**, 589-597.

Hemida, H. and Baker, C. (2010), "Large-eddy simulation of the flow around a freight wagon subjected to a crosswind", *Comput. Fluids*, **39**(10), 1944-1956.

Holmes, J.D. (2001), "Wind loading of parallel free-standing walls on bridges, cliffs, embankments and ridges", *J. Wind Eng. Ind. Aerod.*, **89**(14-15), 1397-1407.

Letchford, C.W. and Holmes, J.D. (1994), "Wind loads on free-standing walls in turbulent boundary layers", *J. Wind Eng. Ind. Aerod.*, **51**(1), 1-27.

Letchford, C.W. and Robertson, A.P. (1999), "Mean wind loading at the leading ends of free standing walls", *J. Wind Eng. Ind. Aerod.*, **79**(1-2), 123-134.

Ministry of Communications of PRC. (2004), S*pecifications on wind resistance design of highway bridges (JTG/T D60-01-2004)*, Beijing, China(in Chinese).

Ogawa, T. and Fujii, K. (1997), "Numerical investigation of three-dimensional compressible flows induced by a train moving into a tunnel", *Comput. Fluids*, **26**(6), 565-585.

Quinn, A.D., Baker, C.J. and Wright, N.G. (2001), "Wind and vehicle induced forces on flat plates - Part 1: wind induced force", *J. Wind Eng. Ind. Aerod.*, **89**(9), 817-829.

Quinn, A.D., Baker, C.J. and Wright, N.G. (2001), "Wind and vehicle induced forces on flat plates - Part 2: vehicle induced force", *J. Wind Eng. Ind. Aerod.*, **89**(9), 831-847.

Robertson, A.P., Hoxey, R.P. and Richards, P.J. (1995), "Design code, full-scale and numerical data for wind loads on free-standing walls", *J. Wind Eng. Ind. Aerod.*, **57**(2-3), 203-214.

Robertson, A.P., Hoxey, R.P., Richards, P.J. and Ferguson, W.A. (1997), "Full-scale measurements and computational predictions of wind loads on free-standing walls", *J. Wind Eng. Ind. Aerod.*, **67-68**, 639-646.

Robertson, A.P., Hoxey, R.P., Short, J.L., Ferguson, W.A. and Blackmore, P.A. (1997), "Wind loads on boundary walls: Full-scale studies", *J. Wind Eng. Ind. Aerod.*, **69-71**, 451-459.

Robertson, A.P., Hoxey, R.P., Short, J.L., Ferguson, W.A. and Osmond, S. (1996), "Full-scale testing to determine the wind loads on free-standing walls", *J. Wind Eng. Ind. Aerod.*, **60**, 123-137.

Sanz-Andrés, A., Laverón, A., Baker, C. and Quinn, A. (2004), "Vehicle induced loads on pedestrian barriers", *J. Wind Eng. Ind. Aerod.*, **92**(5), 413-426.

Sanz-Andrés, A. and Santiago-Prowald, J. (2002), "Train-induced pressure on pedestrians", *J. Wind Eng. Ind. Aerod.*, **90**(8), 1007-1015.

Sanz-Andrés, A., Santiago-Prowald, J., Baker, C. and Quinn, A. (2003), "Vehicle-induced loads on traffic sign panels", *J. Wind Eng. Ind. Aerod.*, **91**(7), 925-942.

Shin, C. and Park, W. (2003), "Numerical study of flow characteristics of the high speed train entering into a tunnel", *Mech. Res. Commun.*, **30**(4), 287-296.

Waymel, F., Monnoyer, F. and William-Louis, M.J.P. (2006), "Numerical simulation of the unsteady three-dimensional flow in confined domains crossed by moving bodies", *Comput. Fluids*, **35**(5), 525-543.

CC